

Corrosion Behavior and Mechanisms of Carbon Steel in the 1,4-Butanediamine/Ethylene Glycol/H₂O CO₂ Capture System

Cunshi Wang, Qiuzi Zhu, Zhimin Gao, Jianzhong Zhu,* Liang Chen, Jianlong Liu, and Wangjun Bai



Cite This: *Energy Fuels* 2023, 37, 14946–14960



Read Online

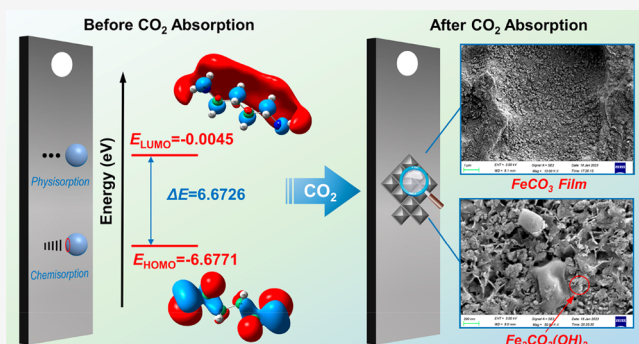
ACCESS |

Metrics & More

Article Recommendations

Supporting Information

ABSTRACT: The chemical absorption of CO₂ using amine aqueous solutions is the most well-established and efficient approach to CCUS technology. However, these solutions can corrode carbon steel infrastructure, impacting production safety and cost-effectiveness. This study identifies a high CO₂ loading (1.2561 mol mol⁻¹) ternary system of 1,4-butanediamine (BDA), ethylene glycol (EG), and 70 wt % H₂O (BE70H). The corrosion behavior and mechanism of BE70H on 20# carbon steel (20CS) were studied by weight loss test, ICP-OES analysis, electrochemical experiment, and various characterization techniques, with 30 wt % MEA solution was selected as a reference. The results show that the CO₂-loaded amine solution is more corrosive to 20CS than the fresh solution. Fresh and CO₂-saturated BE70H solutions (BE70HS) exhibited lower corrosion rates and lower iron concentrations. The characterization results showed that the surface of 20CS corroded by BE70HS formed a dense siderite (FeCO₃) film. This film is believed to provide better corrosion inhibition than the chukanovite (Fe₂CO₃(OH)₂) film formed in MEA-saturated solutions. The quantum chemical parameters, such as E_{HOMO} , E_{LUMO} , and ΔE , indicate that BDA molecules exhibit stronger adsorption on the surface of 20CS compared to MEA, effectively inhibiting the penetration of corrosive agents. The FeCO₃ film and the adsorbed BDA layer on the 20CS surface are considered the major and minor pathways of corrosion inhibition, respectively. Furthermore, the phase separation behavior of the BE70H solution can potentially lead to differences in corrosiveness, making it a critical factor to consider in equipment anticorrosion design.



1. INTRODUCTION

In response to the climate change, over 100 nations have pledged to achieve carbon neutrality by 2050, with China aiming for net-zero CO₂ emissions by 2060.¹ This commitment has accelerated the development of carbon capture, utilization, and storage (CCUS) technologies.² Among various methods, chemical absorption with amine-based solutions is a well-established and efficient technique due to its high selectivity and CO₂ loading capacity.³ However, the significant corrosiveness of aqueous amine solutions poses a challenge.⁴ This corrosivity can damage critical CCUS infrastructure such as absorption towers, stripper towers, and cross-heat exchangers.

While carbon steel is a cost-effective material extensively used in CCUS systems, its lower corrosion resistance compared to that of stainless steel can lead to absorbent degradation and equipment damage.⁵ The corrosion of carbon steel in amine-based CO₂ capture systems is determined by a range of factors, encompassing the choice of amine, the CO₂ absorption loading, and the pH value of the system. For example, studies show that the alkanolamine/RTIL system can decrease the corrosion rate (CR) by about 72% compared to a traditional aqueous amine solution at the same temperature.⁶

Lv et al.⁷ used an immersion test to study the corrosion of carbon steel in the nonaqueous AMP/AEEA/NMP solvent, observing low corrosion levels in both fresh and CO₂-saturated solvents. Wu et al.⁸ evaluated the corrosiveness of the AFIL solution on carbon steel in CO₂ capture applications. The results indicated negligible corrosion in fresh AFIL solutions (with a corrosion rate close to 0 mm a⁻¹), but a significant increase was observed after CO₂ loading. Another study used NaHCO₃ to adjust the pH to 9.3 and 9.1, aiming to evaluate its influence on A106 carbon steel.⁹ The research found that a reduction in pH accelerates the initial carbon steel corrosion. However, a comprehensive study on corrosion is essential to assess the application feasibility of carbon steel in the CO₂ chemical absorption infrastructure.

Received: June 23, 2023

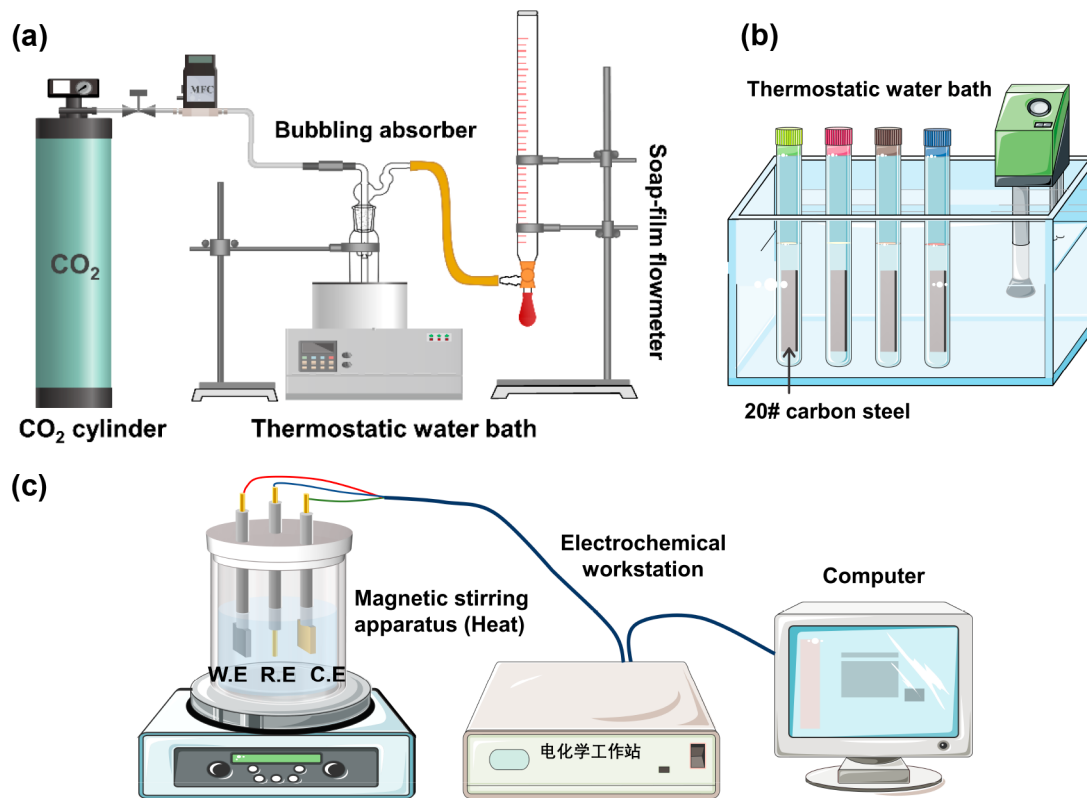
Revised: September 1, 2023

Published: September 26, 2023



Table 1. Main Chemical Composition of 20# Carbon Steel

composition typical wt %	carbon (C)	silicon (Si)	manganese (Mn)	sulfur (S)	phosphorus (P)	chromium (Cr)	<th>copper (Cu)</th> <th>iron (Fe) bal</th>	copper (Cu)	iron (Fe) bal
	0.23	0.31	0.55	0.030	0.028	0.21	0.18	0.16	

**Figure 1.** Experimental apparatus schematic for (a) the CO_2 bubbling absorption, (b) the immersion corrosion test, and (c) the electrochemical corrosion test.

Corrosion can be effectively inhibited if a dense protective film is formed on the carbon steel surface after exposure to CO_2 -loaded amine solution.¹⁰ These films act as a physical barrier that minimizes contact between the carbon steel substrate and solution, offering further corrosion protection. Scanning electron microscopy (SEM) and X-ray diffraction (XRD) have identified that these films are composed of various components, including siderite (FeCO_3),¹¹ goethite ($\alpha\text{-FeOOH}$),¹² chukanovite ($\text{Fe}_2\text{CO}_3(\text{OH})_2$),¹³ or a combination thereof. Pandarinathan et al.¹⁴ revealed $\text{Fe}_2\text{CO}_3(\text{OH})_2$ as the main component of the corrosion layer on sand-deposited carbon steel in CO_2 -saturated brine at 80 °C. Zheng et al.¹⁵ found through short-term corrosion studies that the corrosion rate of A106 carbon steel in 30 wt % piperazine (PZ) was lower than in 30 wt % MEA under the same conditions. This is because the surface of carbon steel in the PZ solution can form a dense, protective FeCO_3 layer. FeCO_3 is considered a more stable corrosion product on the surface of carbon steel than $\text{Fe}_2\text{CO}_3(\text{OH})_2$ and can effectively protect the underlying steel from further corrosion.¹⁶ Carbonate and bicarbonate dominate protective film formation as the products of the CO_2 absorption. However, the potential anticorrosion effects of amines themselves are often overlooked; they can inhibit the corrosion of carbon steel before CO_2 absorption. This inhibition is mainly due to their adsorption onto the protected metal surface, forming a hydrophobic film that blocks aggressive ions.¹⁷ Understanding the characteristics of the

protective film and the corrosion-inhibiting properties of the amine itself can facilitate optimizing the design of CO_2 absorption equipment and amine solutions. Such optimization has the potential to extend the life span of the equipment and reduce operational costs.

The formation of solids after absorption by nonaqueous amine/alcohol solvents developed in our previous work has limited its practical application.¹⁸ However, the ternary system of amine/alcohol/ H_2O can avoid solid formation and offers high CO_2 absorption rates, large capacities, and reduced energy needs for regeneration.^{19,20} This study screened the BDA/EG/ H_2O ternary system with high CO_2 loading as the corrosive medium of 20# carbon steel (20CS). The corrosion behavior was comprehensively investigated by using weight loss tests, ICP-OES analysis, electrochemical measurements, and other characterization techniques. An aqueous solution of 30 wt % MEA was utilized as a comparative reference. Furthermore, the quantum chemical parameters, such as the highest occupied molecular orbital energy (E_{HOMO}), lowest unoccupied molecular orbital energy (E_{LUMO}), energy gap (ΔE), and dipole moment (μ), were used to elucidate the corrosion inhibition effect of BDA and MEA on 20CS. The corrosion and inhibition mechanisms of 20CS in a BDA/EG/ H_2O solution are presented based on experimental and computational results. The primary objective of this research is to offer essential theoretical data for the potential industrial application

of the BDA/EG/H₂O system, rather than comparing it with the nonaqueous BDA/EG solvent.

2. EXPERIMENTAL SECTION

2.1. Chemicals. The 20# carbon steel (20CS) used in this study was procured from Hefei Wenhui Metal Material Limited; its chemical composition is shown in Table 1. Carbon dioxide (CO₂, 99.99%) was provided by Nanjing Wenda Special Gas Co., Ltd., China. All chemicals, including 1,4-butanediamine (BDA, AR, 98%) and monoethanolamine (MEA, AR, 99%), were obtained from Shanghai Aladdin Biochemical Technology Co., Ltd., and are detailed in Table S1.

2.2. Experiments. 2.2.1. *CO₂ Absorption.* The schematics of the CO₂ bubbling absorption apparatus are presented in Figure 1a. In each experiment, 30 mL of absorbents was added to a 100 mL custom reactor. The system was maintained at 313.15 K using a water bath, and CO₂ was bubbled in at 150 mL min⁻¹. Effluent flow was measured using a soap film flowmeter at 60 s⁻¹ intervals. The absorption rate (r_{abs}) and total CO₂ loading (T_L) were calculated using eqs 1 and 2.

$$r_{\text{abs}} = \frac{Q_{\text{in}} - Q_{\text{out}}}{22.4 \times 1000} \left(\frac{P_{\text{act}} T_0}{P_0 T_{\text{act}}} \right) \quad (1)$$

$$T_L = \frac{\int_0^t r_{\text{abs}} dt}{n_{\text{amine}}} \quad (2)$$

Herein, r_{abs} is the CO₂ absorption rate (mol min⁻¹), Q_{in} and Q_{out} are the inlet and outlet CO₂ flow rates (mL min⁻¹), P_{act} and P_0 are the atmospheric pressures under actual and standard states (101.325 kPa), T_{act} and T_0 are the temperatures at 313.15 and 273.15 K, T_L is the total CO₂ loading of the solvent (mol mol⁻¹), n_{amine} is the mole quantity of amine, and t is the absorption time (min).

2.2.2. *Immersion Corrosion Test.* The dimensions of the 20CS corrosion coupons were 72.4 mm × 11.5 mm × 2 mm. The coupons underwent initial soaking in dilute hydrochloric acid (18 wt %) for 30 s to remove small amounts of corrosion products and organic contaminants.²¹ They were polished with SiC sandpaper (800/1000/1200 grit) and then sequentially washed with deionized water, ethanol, and acetone before oven-drying at 313.15 K. The cleaned and preweighed coupons were soaked in a corrosive medium at 313.15 K for 144 h. After the immersion corrosion experiment, the sample was rinsed with pickling acid, deionized water, and acetone and then dried and weighed again. The corrosion rate (CR) for 20CS was calculated using eq 3. The immersion test apparatus is depicted in Figure 1b.

$$\text{CR} = \frac{87600(m_0 - m)}{A\rho t} \quad (3)$$

Here, CR denotes the corrosion rate (mm a⁻¹), m_0 and m are the initial and final weights (g), A is the exposed surface area (cm²), ρ is the coupon density (g cm⁻³), and t is the corrosion time (h). The constant 87600 is for unit conversion.

2.2.3. *Electrochemical Measurements.* Electrochemical evaluations were performed on a CHI602E workstation provided by Chenhua Instrument Co., Ltd., Shanghai. The experiment apparatus, shown in Figure 1c, utilized a 50 mL three-electrode cell containing a 20CS working electrode, a Ag/AgCl reference electrode (saturated KCl), and a platinum counter electrode. The working electrode, with dimensions of 20 × 10 × 2 mm³, was embedded in epoxy, exposing only one 20 × 10 mm² face (exposed area of 2 cm²) to the test amine-based solution. The specimens stabilized at an open circuit potential (OCP) before undergoing electrochemical impedance spectroscopy (EIS) measurements at the OCP with 10 mV amplitude signals across frequencies ranging from 10⁵ to 10⁻² Hz. Tafel curves spanned from -250 to +250 mV relative to the OCP at a scan rate of 0.16 mV s⁻¹. CR was derived from the corrosion current density (i_{corr}) via Tafel extrapolation, as detailed in eq 4.

$$\text{CR} = \frac{3.27 \times 10^{-3} i_{\text{corr}} W}{A \rho} \quad (4)$$

Here, W is the equivalent weight of the 20CS (g equiv⁻¹), A is the exposed surface area (cm²), and ρ denotes the density (g cm⁻³). The conversion constant used is 3.27 × 10⁻³.

2.3. Analysis Methods. 2.3.1. *ICP-OES Analysis.* The iron concentration in the test solution was quantified using inductively coupled plasma optical emission spectrometry (ICP-OES, Agilent 5110). A 0.1 g sample was digested in a mixture of 5 mL of nitric acid and 1 mL of hydrofluoric acid at 190 °C for 10 h. After cooling, the test solution was placed in a 25 mL flask and diluted with deionized water. Each solution underwent three measurements to obtain an average value.

2.3.2. *Characterization Analysis.* Scanning electron microscopy (SEM, ZEISS Sigma 300, Germany) was conducted at 20 kV and 20 μA to observe the surface features of the 20CS coupons. For chemical composition analysis, energy-dispersive spectroscopy (EDS, Xplore 30, Oxford Instruments, Germany) was used (working distance: 10 mm; voltage: 20 kV).

Grazing incidence X-ray diffractograms were obtained by using a Rigaku SmartLab with a Cu Kα source (45 kV, 200 mA). Data were captured over a 2θ range of 10°–115°, with a 0.04° step size and 2° min⁻¹ scan rate. Phase identification employed the Bragg–Brentano mode on a Bruker D8 Advance A2S (40 kV, 40 mA, Lynx Eye XE-T detector) for sample roughness that impeded data alignment. Data analysis was performed with MDI Jade 9.5 software.

¹³C NMR analysis of the CO₂ absorption products was conducted on a 500 MHz NMR spectrometer (AVANCE III, Bruker, Germany). A mixture of 400 μL of sample, 10 μL of 1,4-diazole as an internal standard, and 100 μL of D₂O for field locking was prepared. Parameters were set as follows: resonance frequency 100.63 MHz, excitation power 95.10 W, and acquisition time 1.38 s with 512 scans. Data were processed using ACD-LAB and MestReNova software.

The 2D and 3D morphologies of corroded 20CS were captured by using a commercial atomic force microscope (AFM, Dimension ICON, Bruker, Germany) system at room temperature. A suitable 20CS sample was chosen and sized for the AFM stage. The sample was ultrasonically cleaned with acetone or isopropanol for 5–10 min and then dried with N₂. After cleaning, the sample was positioned on the AFM stage for imaging.

2.4. *Quantum Chemical Calculations.* Density functional theory (DFT) calculations were performed using the Gaussian 16W software package, employing the B3LYP/6-311++G (d,p) basis set to serve as a robust method for investigating the relationships between the molecular characteristics of inhibitors and their inhibition efficiencies. This study focused only on individual molecules; therefore, the calculations did not include dispersion effects. Solvent effects were assessed using the general implicit solvation model, solvent model density (SMD). Quantum chemical computations were conducted in the aqueous phase to simulate the actual corrosion system conditions. The highest occupied and lowest unoccupied molecular orbital (HOMO and LUMO) parameters were used to evaluate the anticorrosion properties of the amines studied. The analysis included the energy gap (ΔE), dipole moment (μ), electronegativity (χ), global hardness (η), global softness (σ), and the fraction of electrons transferred (ΔN). The calculation used the following equations:

$$\Delta E = E_{\text{LUMO}} - E_{\text{HOMO}} \quad (5)$$

$$\chi = -\frac{1}{2}(E_{\text{LUMO}} + E_{\text{HOMO}}) \quad (6)$$

$$\eta = \frac{1}{2}(E_{\text{LUMO}} - E_{\text{HOMO}}) \quad (7)$$

$$\Delta N = \frac{\chi_{\text{Fe}} - \chi_{\text{inh}}}{2(\eta_{\text{Fe}} + \eta_{\text{inh}})} \quad (8)$$

In eq 8, χ_{Fe} and χ_{inh} refer to the absolute electronegativity of iron and the inhibitor while η_{Fe} and η_{inh} represent their respective absolute hardness. Theoretical values for χ_{Fe} and η_{inh} are 7 eV mol⁻¹ and 0 eV mol⁻¹ for bulk iron.²²

3. RESULTS AND DISCUSSION

3.1. Tricomponent Solution Screening. Nonaqueous amine/alcohol absorbents are recognized as promising candidates for CO₂ capture. This study employs three common amines (BDA, TETA, and PZ) and four alcohols (EtOH, EG, 1,4-BDO, and 1-propanol) to examine the phase separation behavior and CO₂ loading in amine/alcohol combinations (with a molar ratio of 1:2) and then further screen out the efficient ternary H₂O system.

In most nonaqueous amine/alcohol absorbents, liquid–solid phase separation was observed after CO₂ adsorption, as shown in Table 2, which is consistent with previous studies.²³ Figure

Table 2. Phase Separation Behavior of Nonaqueous Solvents after CO₂ Absorption^a

amine/alcohol	ethanol	ethylene glycol	1,4-butanediol	1-propanol
BDA	Y	Y	Y	Y
TETA	Y	N	N	N
PZ	Y	Y	Y	N

^a Y denotes liquid–solid phase separation, while N denotes no liquid–solid phase separation.

2a shows that BDA/EG had the highest CO₂ loading of 0.9039 mol mol⁻¹. The higher CO₂ loading was attributed to two key factors: BDA's elevated alkalinity increases its reactivity with CO₂, and the presence of BDA allows EG to form alkyl carbonate as an alternative pathway for CO₂ fixation.²⁴ Therefore, further investigations focused on the BDA/EG mixture. However, the formation of solids after CO₂ absorption (Table 2 and Figure S2), while potentially beneficial for energy conservation during regeneration, introduces complexity to phase separation and risks pipeline blockage in practical applications.²⁵ Adding H₂O to the nonaqueous absorbent is expected to avoid solid phase formation and further increase the CO₂ loading of the system.

Firstly, H₂O helps curb a potential increase in solution viscosity after CO₂ absorption, thereby effectively preventing

the precipitation of products in the CO₂-rich solution.^{26,27} Secondly, it can promote carbamate hydrolysis, thus significantly increasing the absorption capacity.²⁸ In addition, research has shown that mixtures of alcohol and H₂O, when used as solvents, demonstrate high absorption efficiency, efficient desorption, and lower energy loss during regeneration.²⁰ Given this, the study examined the influence of H₂O content on phase separation and CO₂ loading in nonaqueous BDA/EG solvent. The findings show that BDA/EG/H₂O solutions with over 30 wt % H₂O contents exhibit no liquid–solid phase separation after CO₂ absorption, and the solution remains clear. The presence of H₂O significantly increased the CO₂ loading of the BDA/EG solvents. As shown in Figure 2b, the CO₂ loading reached 1.3622 mol mol⁻¹ with an H₂O content of 80%, reflecting a 50.32% increase compared to the BDA/EG. Furthermore, the CO₂ loading of both nonaqueous and aqueous BDA/EG outperformed that of a MEA solution. In general, a lower H₂O content results in a higher viscosity of the absorbent, which makes pipeline pumping more difficult, whereas an excessively high H₂O content can increase the heat capacity of the absorbent, thereby increasing regeneration energy consumption. Considering the trade-off between the CO₂ loading, regeneration energy, and industrial applicability, an optimal H₂O content of 70% was determined. Therefore, the BDA/EG/70 wt % H₂O (BE70H) solution with a CO₂ absorption loading of 1.2561 mol mol⁻¹ was chosen for further corrosion studies.

3.2. Corrosion Rate of Carbon Steel. Corrosion in the equipment is a crucial factor in choosing chemical solvents for CO₂ capture. The corrosion behavior of 20CS coupons in various amine solutions, including fresh and saturated CO₂ solutions, was evaluated by weight loss tests and ICP-OES analysis. Table 3 provides the details and abbreviations of these amine-based solutions.

Corrosion rates (CR) were derived from the mass changes in 20CS coupons submerged in the absorbent. The iron concentrations in these solutions was then determined using ICP-OES. Figure 3 illustrates a correlation between CR and the iron concentration in the amine-based solution, confirming the validity of the weight loss test. The low iron concentrations and CR values in MEA, B1E2, BE70H, and B70H solutions suggest minimal corrosiveness in their fresh states. The B70H

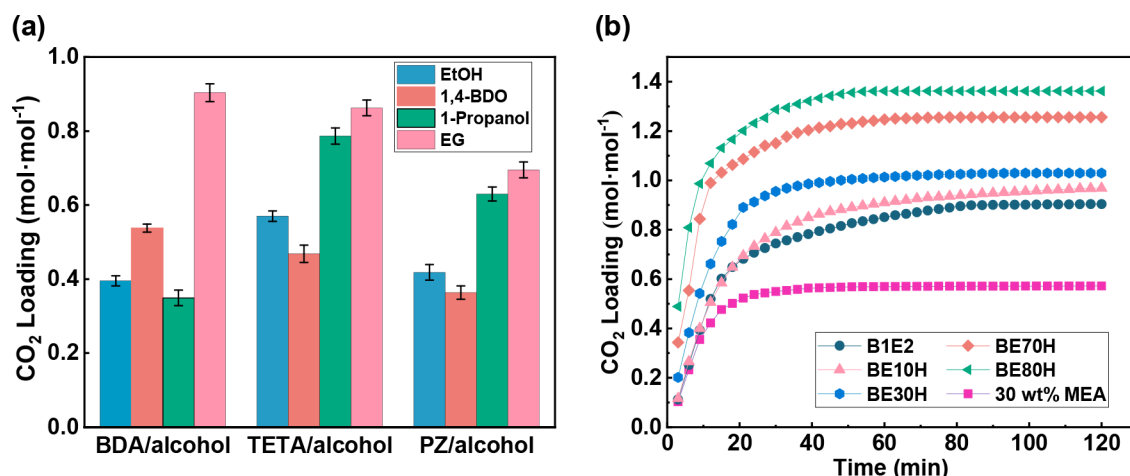


Figure 2. CO₂ absorption loading of mixed solutions: (a) amine/alcohol systems; (b) BDA/EG/H₂O systems. Data for the B1E2 system are sourced from our previous work¹⁸ ($m = 30$ g, $Q_{\text{in}} = 150$ mL min⁻¹, $t = 90$ min, $T_{\text{abs}} = 313.15$ K).

Table 3. Solutions Used in Corrosion Experiments and Their Abbreviations

type	solution composition	abbreviation
fresh solution	30 wt % MEA + 70 wt % H ₂ O	MEA
	BDA/EG biphasic solvent with a molar ratio of 1:2	B1E2
	30 wt % BE70H + 70 wt % H ₂ O	BE70H
	30 wt % B70H + 70 wt % H ₂ O	B70H
CO ₂ -loaded solution	BE70H solution after 6 min of CO ₂ injection	BEH6
	BE70H solution after 12 min of CO ₂ injection	BEH12
	BE70H solution after 24 min of CO ₂ injection	BEH24
	CO ₂ -saturated BE70H solution	BEHS
	CO ₂ -saturated 30 wt % MEA solution	MEAS

solution exhibited the lowest concentration of iron and showed the lowest CR for 20CS, recorded as 0.12 mg L^{-1} and 0.0077 mm a^{-1} , respectively. The BE70H fresh solution of concern in this study also showed low corrosion, with iron concentration and CR values of 0.14 mg L^{-1} and 0.0079 mm a^{-1} , respectively. In the CO₂-loaded state, both amine systems (BE70H, MEA) demonstrated a significant increase in iron concentration and CR. The MEAS solution reached peak values of 38.75 mg L^{-1} and 0.2791 mm a^{-1} , significantly surpassing the peak values observed in the BEHS solution.

Figure 3a shows that among the fresh solutions (MEA, B1E2, BE70H, B70H), B1E2, a nonaqueous solvent, exhibited the highest iron ion concentration and CR, measured at 0.2 mg L^{-1} and 0.0081 mm a^{-1} , respectively. The reasons for this could be: the high alkalinity of BDA can cause alkali corrosion, and the high concentration of EG in solution may accelerate it.²⁹ However, in amine aqueous solutions such as BE70H, MEA, and B70H, the presence of H₂O might reduce corrosiveness. First, H₂O can serve as a neutralizer, counteracting BDA's high alkalinity and, thus, reducing the risk of alkali-induced corrosion. Second, H₂O could reduce the conductivity, potentially decelerating the rate of electrochemical reactions linked to corrosion. Third, under certain conditions, H₂O could aid in forming or maintaining a passivation layer on the carbon steel surface and protecting against corrosion. B70H exhibits less corrosiveness to 20CS than MEA at equivalent amine concentrations. Some studies suggest that amines can act as corrosion inhibitors;³⁰ considering this, BDA might possess superior corrosion inhibitory efficiency compared to MEA. Figure 3b shows that

upon CO₂ loading, BE70H experiences an increase in both iron concentration and CR. The increased solution corrosivity toward 20CS can be ascribed to forming bicarbonate and carbamate compounds.⁸ Notably, with a CO₂ loading of $1.2561 \text{ mol mol}^{-1}$, the BEHS solution exhibits a CR of 0.2001 mm a^{-1} on 20CS, significantly lower than MEA's. These findings suggest that BE70H can reduce equipment corrosion and improve CCUS system capture efficiency compared to MEA.

3.3. Electrochemical Corrosion Behavior. 3.3.1. Tafel Curve. Electrochemical experiments were conducted to measure the corrosion behavior of 20CS in various solutions. Compared to the weight-loss test, the Tafel curve offers a quicker and more precise method for calculating the corrosion rate (CR) over a specific time. Figure 4 presents Tafel plots

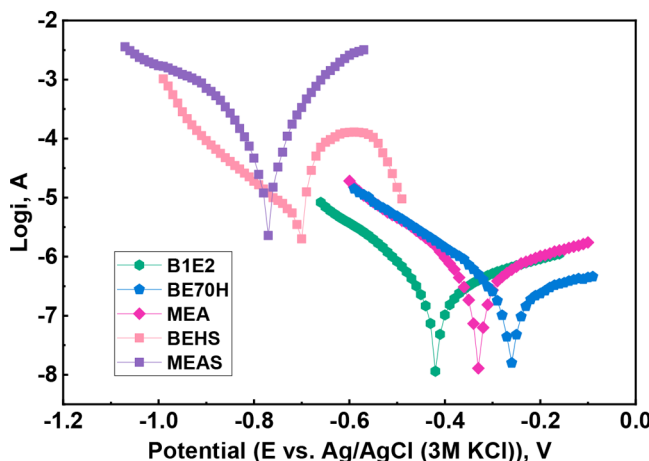


Figure 4. Tafel curves for 20CS working electrode in different test solutions ($T = 313.15 \text{ K}$).

derived from anodic polarization tests in both fresh and CO₂-loaded amine solutions at 313.15 K . Solution abbreviations are detailed in Table 3. Table 4 compiles key electrochemical parameters: corrosion current density (i_{corr}), corrosion potential (E_{corr}), anodic Tafel slope (β_a), cathodic Tafel slope (β_c), and CR. Because of the liquid–solid phase change in B1E2 after CO₂ absorption,¹⁸ the CO₂-saturated B1E2 solvent is not included in this discussion.

Figure 4 presents Tafel plots for three fresh solutions (B1E2, BE70H, and MEA), all displaying a consistent smooth pattern within a specific potential range. A linear relationship is evident

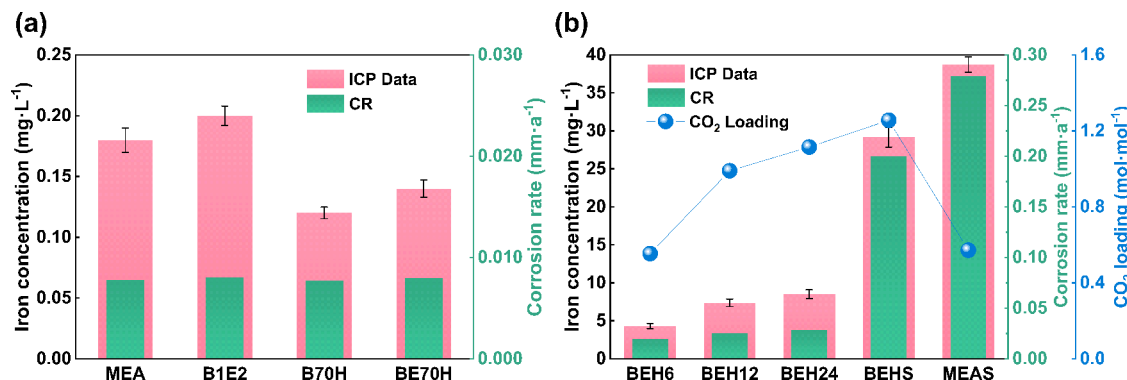


Figure 3. Iron concentration and corrosion rate in different amine solutions after weight loss test: (a) fresh solutions; (b) CO₂-loaded solutions.

Table 4. Corrosion Parameters of 20CS in Different Amine-Based Solutions

solutions	corrosion parameters					
	$-E_{OCP}$ (mV)	$-E_{corr}$ (mV)	i_{corr} (μ A)	β_a (mV/dec)	$-\beta_c$ (mV/dec)	CR (mm a ⁻¹)
B1E2	420	414	0.16	226	123	0.001
BEH	260	261	0.15	287	132	0.001
MEA	330	341	0.32	238	119	0.002
BEHS	700	844	39.26	488	145	0.228
MEAS	770	776	45.52	87	96	0.265

between the logarithm of current density and potential. This suggests that the activation process predominantly governs the anodic and cathodic reactions rather than the rate of reactant transfer to the electrode surface. This characteristic is typical of active corrosion, which strongly correlates with the CR and reaction kinetic parameters such as activation energy. While the adsorption of amines on the 20CS surface might form a protective layer, it does not offer complete inhibition against the dissolution or redox reactions of metal ions. Furthermore, in these fresh solutions (refer to Table 4), the more significant Tafel slope value of β_a relative to β_c indicates a predominantly anodic control of 20CS corrosion. The CR of 20CS in saturated solutions (BEHS and MEAS) significantly higher than in fresh solutions. This increase might be partly due to carbamate formation after absorption, which enhances conductivity and speeds up ion transport, thereby accelerating CR.³¹ Additionally, the corrosion may be promoted by amines, protonated amine ions, and carbamate ions disrupting the protective film on the 20CS surface.¹² Table 4 shows similar corrosion potentials for 20CS electrodes in both BEHS and MEAS, indicating a comparable corrosion mechanism in both solutions for 20CS. For BEHS, β_a is greater than β_c , while in MEAS, β_a is less than β_c , suggesting that anodic and cathodic reactions control the corrosion of 20CS in these solutions. Importantly, both anodic and cathodic corrosion current densities are lower in the BEHS solution than in the MEAS solution (Figure 4). This implies more effective hindrance of both anodic and cathodic reactions in the BEHS solution due to the reactants' transfer rate to the working electrode surface. This phenomenon could be attributed to the development of a more effective protective film on the 20CS surface upon exposure to the BEHS solution, consequently resulting in corrosion mitigation.

The Tafel plot analysis reveals low CRs for fresh solutions, all below 0.002 mm a⁻¹. The corrosion of the saturated solution to 20CS was significantly increased with CR values of 0.228 mm a⁻¹ for BEHS and 0.265 mm a⁻¹ for MEAS. These findings are consistent with the results from the weight loss test. Table 5 contrasts the CO₂ loading and CR of BEHS and MEAS solutions to other amine aqueous solutions. The BE70H exhibits relatively low CR and the highest CO₂ loading, providing significant advantages for industrial applications.

3.3.2. Electrochemical Impedance Spectroscopy (EIS). EIS is a nondestructive method that swiftly characterizes and evaluates corrosion behavior, offering comprehensive insights. EIS experiments assessed the corrosion properties of 20CS in fresh and CO₂-saturated solutions and the electrochemical interactions at the metal–solution interface. Figure 5 presents the Nyquist and Bode diagrams of 20CS in both fresh and CO₂-saturated solutions.

Table 5. Corrosion Rates of 20CS in Different Amine-Based Solutions after CO₂ Absorption

test medium	CO ₂ loading (mol mol ⁻¹)	T (°C)	type of steel	CR (mpy ^a)	ref
BEHS	1.2286	40	20# carbon steel	8.98	this work
MEAS	0.5719	40	20# carbon steel	10.441	this work
0.2 mol/L PZ aqueous	0.82	20	20# carbon steel	280.67	31
DEA/IL emulsion	0.5	60	carbon steel	0.31	32
15 wt % DEA aqueous		60	carbon steel	289.82	32
8 m PZ aqueous	0.21	160	carbon steel 1010	0.69	10
MEA aqueous	0.5	60–65	carbon steel	10–15	33
AMP aqueous	0.17	25	carbon steel 1020	9.8	34
5 kmol m ⁻³ PZ aqueous	0.82	80	carbon steel 1018	16.4	35
30 wt % MEA aqueous			carbon steel	19.23	36
20 wt % MEA aqueous			carbon steel	33.02	37
MEA/PZ = 7:1.7 (mole ratio)	0.2	80	carbon steel 1018	37.25	38
3 kmol m ⁻³ MDEA aqueous	0.243	80	stainless steel	67.6	39

^aThe conversion factor between CR in mm a⁻¹ and mpy is 39.4.

Figure 5a shows three distinct semicircles in the Nyquist plot for fresh solutions (B1E2, BE70H, and MEA), encompassing real and imaginary impedance vector data. The presence of a semicircle, perfect or not, in the Nyquist plot signifies charge transfer impedance, indicating the central role of charge transfer in these electrochemical processes.⁴⁰ However, the imperfect nature of the observed semicircle implies influences from various factors on the charge transfer process, such as electrolyte ions diffusion, electrode surface heterogeneity, and surface corrosion products. Such factors can contribute to nonideal capacitive behavior, impacting the Nyquist plot shape.⁴¹ A reduced semicircle diameter in Figure 5b suggests decreased charge transfer impedance in CO₂-saturated solutions. This could indicate accelerated corrosion due to enhanced electron transfer to the electrolyte. The impedance radius of the CO₂-loaded solution displays noticeable Warburg impedance characteristics. This could be due to the increased concentration of chemically adsorbed species on the 20CS surface in the CO₂-loaded solution.⁴² As shown in Figure 5c, the impedance modulus |Z| of the three fresh solutions displays relatively high values in the low-frequency band, suggesting a dominant influence of the diffusion process at this stage. In Figure 5d, the BE70H solution exhibits the lowest |Z| value in the high-frequency range, potentially indicating higher ion activity that could accelerate charge transfer and lower impedance. Figure 5e,f shows phase angles decreasing to 0° at high frequencies for all samples, accompanied by a minor peak at low frequencies. This indicates the dominance of resistive processes at high frequencies, reflecting the impact of electrolyte and electron transfer resistances between electrodes. These observations underscore the complex electro-

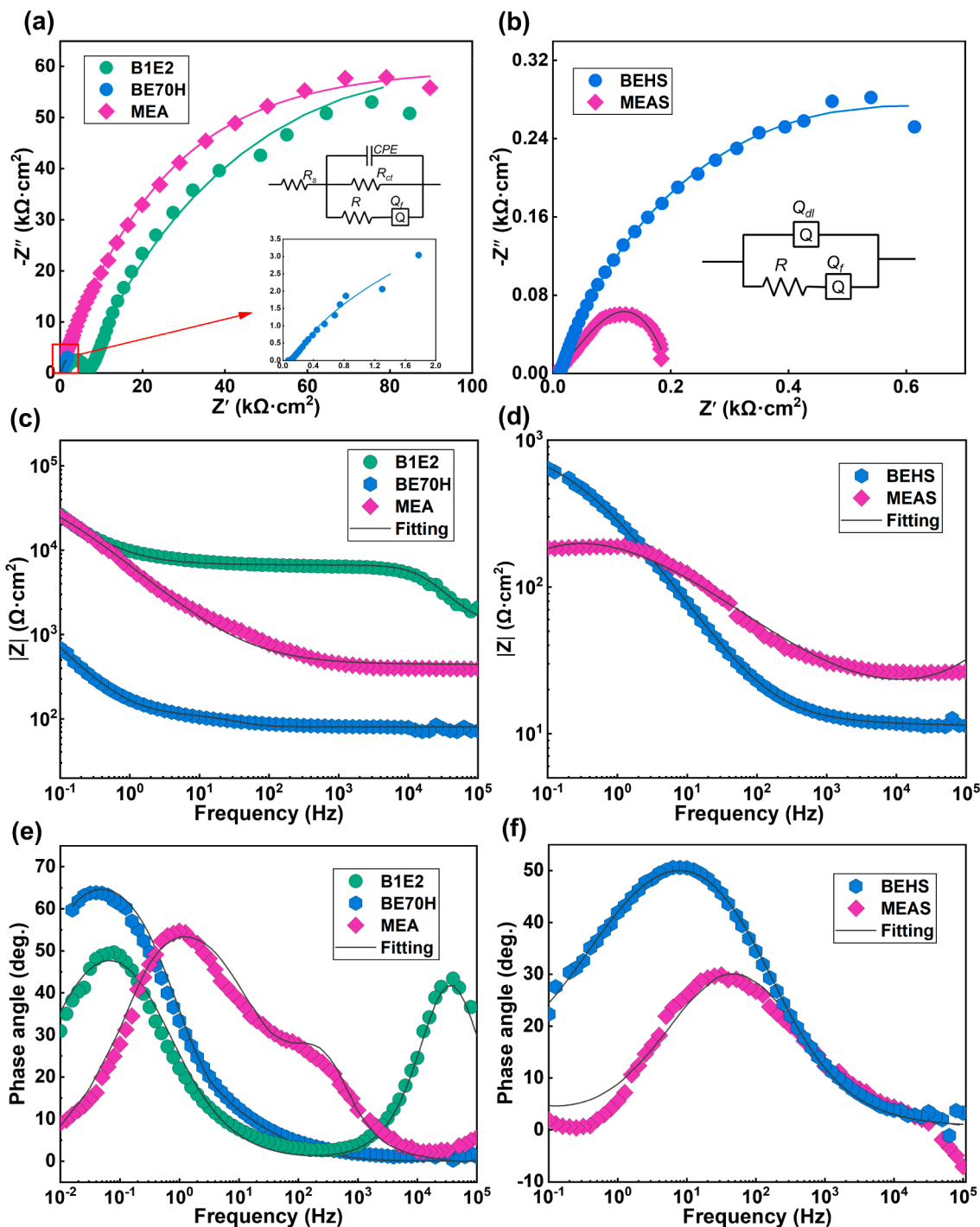


Figure 5. EIS Nyquist and Bode diagrams of 20CS in fresh solutions (a, c, e) and CO_2 -saturated solutions (b, d, f). Nyquist plots (a, b) insets represent the equivalent electrical circuit identifying and fitting EIS diagrams. (c, d) Bode modulus plots and (e, f) Bode phase angle plots.

chemical behavior of 20CS across various frequencies. Furthermore, the decrease in absolute impedance $|Z|$ and phase angle in CO_2 -saturated solutions, as indicated in Figure 5c,e, compared to fresh solutions displayed in Figure 5d,f, may be a result of an increased number of active charge transfer sites.

In the $Q(RQ)$ fitting circuit for CO_2 -saturated solutions, Q_{dl} denotes the constant phase element (CPE), indicative of the double-layer capacitance. The R stands for charge transfer resistance, and Q_f stands for capacitance associated with film formation on the 20CS surface. Table 6 shows that the R value

for the BEHS solution in a CO_2 -saturated environment is larger, suggesting slower electrochemical reaction rates and resulting in lower CR values. Furthermore, the Q_f value for the BEHS solution dramatically exceeds that of the MEAS solution. This suggests that using BEHS results in a thicker or denser surface film on 20CS, enhancing charge transfer resistance and potentially improving corrosion resistance.

3.4. Characterization of Carbon Steel. To gain further insight into the corrosion behavior of 20CS in different solutions, we employed XRD, SEM, and EDS to analyze the surface morphology and element distribution of the coupons

Table 6. EIS Parameters $R(\text{CR}(\text{QR}))$ and $Q(\text{RQ})$ of the Equivalent Circuit Were Fitted to Analyze the Corrosion Behavior of 20CS in Different Solutions

solutions	$R_s (\Omega \text{ cm}^2)$	$C \times 10^{-5} (\mu\text{F cm}^{-2})$	$R_{ct} \times 10^4 (\Omega \text{ cm}^2)$	$Q_f (\Omega^{-1} \text{ cm}^{-2} \text{ s}^{-n})$		$R (\Omega \text{ cm}^2)$	χ^2
				$Q_0 \times 10^{-5}$	n		
B1E2	1335	18.48	18.12	5.324	0.7351	5513	4.568×10^{-3}
BE70H	80.34	0.017	1.356	202.7	0.8148	35.43	4.177×10^{-3}
MEA	378	0.27	1.163	4.165	0.73	712	4.011×10^{-3}
solutions	$Q_{dl} (\Omega^{-1} \text{ cm}^{-2} \text{ s}^{-n})$		$R (\Omega \text{ cm}^2)$	$Q_f (\Omega^{-1} \text{ cm}^{-2} \text{ s}^{-n})$		χ^2	
	$Q_0 \times 10^{-3}$	n		$Y_0 \times 10^{-4}$	n		
BEHS	1.234	0.1074	12.11	6.657	0.7025	6.145×10^{-4}	
MEAS	3.712	0.02	10.19	1.014	0.7164	4.742×10^{-3}	

after the weight loss test. The XRD spectra of 20CS coupons postcorrosion in both CO_2 -saturated solutions, namely BEHS and MEAS, can be seen in Figure 6. Corresponding SEM

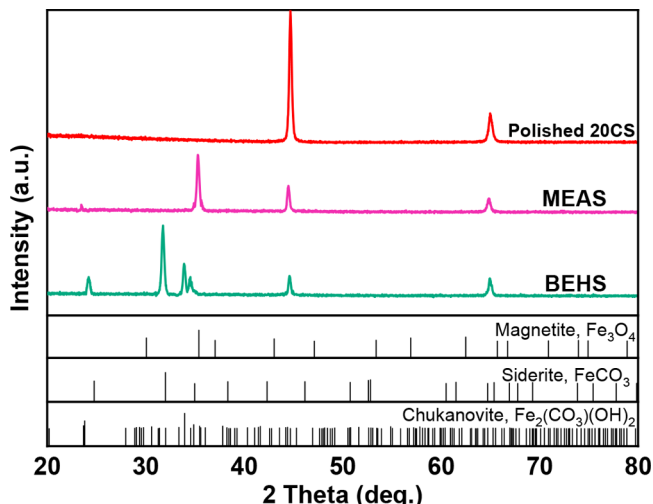


Figure 6. XRD spectra of 20CS after corrosion in BEHS and MEAS solutions.

images of the surface and EDS analysis results are displayed in Figure 7. After 144 h of immersion in a CO_2 -saturated solution, characterization revealed a protective film on the surface of the 20CS coupons. This occurs because after absorption, carbonate (CO_3^{2-}) and bicarbonate (HCO_3^-) species form in the solution. These species then react with the ferrous ions (Fe^{2+}) dissolved from the carbon steel, producing various corrosion products such as siderite (FeCO_3), chukanovite ($\text{Fe}_2\text{CO}_3(\text{OH})_2$), and magnetite (Fe_3O_4).⁴³ The accumulation of these compounds on the 20CS surface forms a dense protective film, which mitigates further corrosion.

Figure S1 depicts the surface morphology of the polished 20CS. It can be observed that prior to exposure to the corrosive solution, the surface of 20CS exhibits a smooth texture with no significant cracks or defects. As depicted in Figure 7, the surface texture of the 20CS coupon turns rough postcorrosion, displaying noticeable corrosion products. The XRD analysis results (Figure 6) suggest that the main corrosion product on the 20CS coupon surface in the BEHS solution is FeCO_3 , while $\text{Fe}_2\text{CO}_3(\text{OH})_2$ and Fe_3O_4 were identified as secondary products. The SEM analysis further confirms that the surface of the 20CS coupon is covered with a dense layer of granular siderite crystals (Figure 7a,b), exhibiting no obvious film defects and randomly interspersed

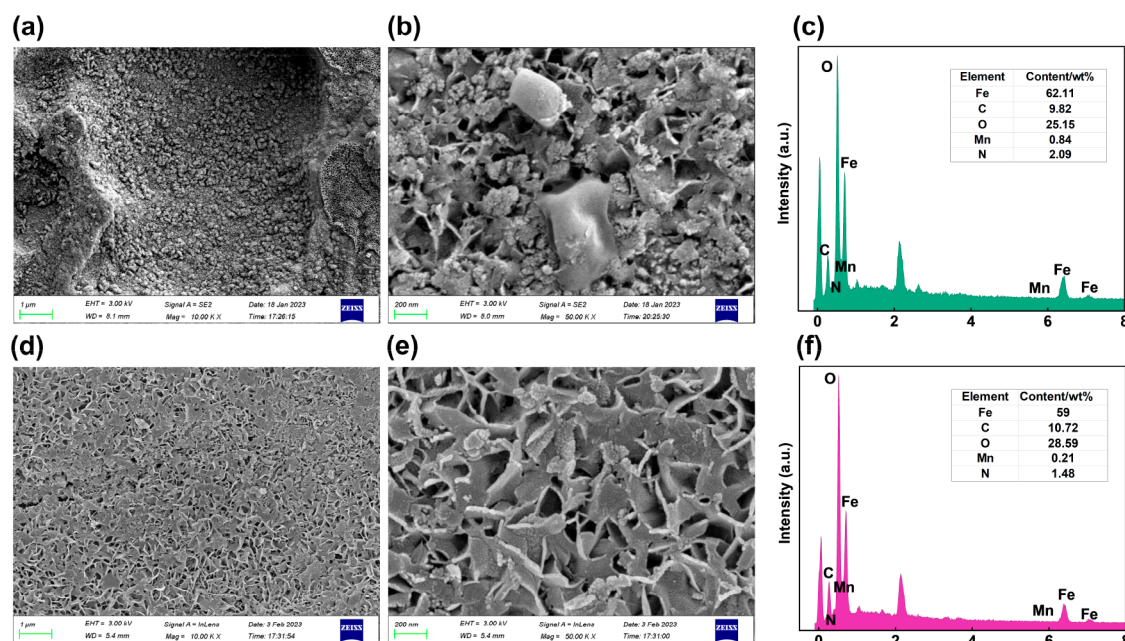
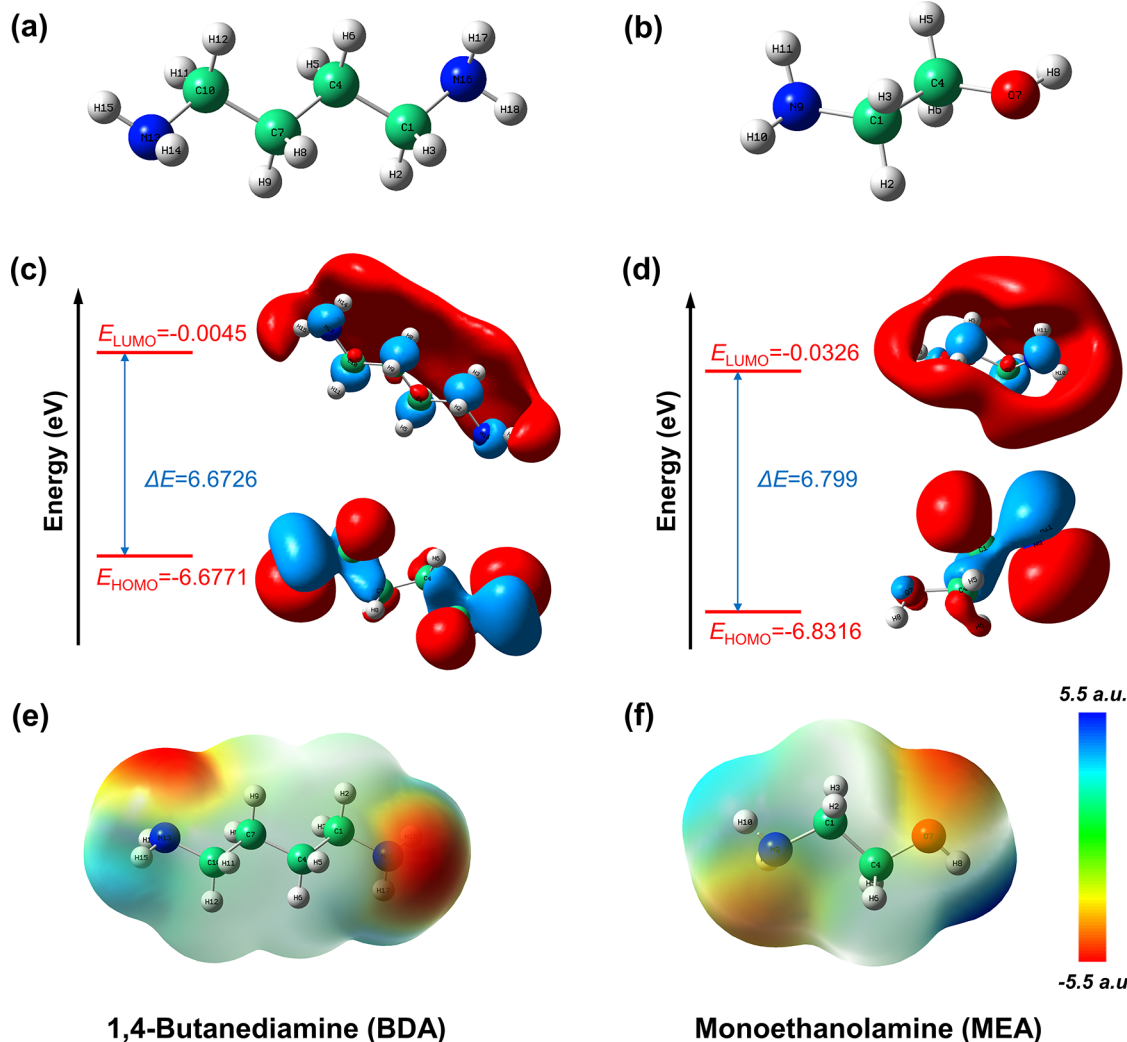


Figure 7. SEM images and EDS spectra of the 20CS surface after corrosion in different solutions: BEHS (a–c) and MEAS (d–f).



1,4-Butanediamine (BDA)

Monoethanolamine (MEA)

Figure 8. Optimized geometry (a, b), HOMO and LUMO (c, d), and MEP (e, f) of BDA and MEA obtained by the B3LYP/6-311++G (d,p) level of basis set in the aqueous phase.

with leaf-like clusters of $\text{Fe}_2\text{CO}_3(\text{OH})_2$. In addition, $\text{Fe}_2\text{CO}_3(\text{OH})_2$ is an intermediate metastable corrosion product that transforms into the more stable FeCO_3 under hypoxic conditions.¹⁶ Figure 7b shows the coexistence of a small number of $\text{Fe}_2\text{CO}_3(\text{OH})_2$ crystals (layered structure) and FeCO_3 crystals (globular nodules), suggesting that this transformation may be underway. For the 20CS coupon corroded in the MEAS solution, the primary corrosion products were identified as $\text{Fe}_2\text{CO}_3(\text{OH})_2$ and Fe_3O_4 , while FeCO_3 was considered to be a trace corrosion product, as shown in Figure 6. The SEM images (Figure 7c,d) also demonstrate that $\text{Fe}_2\text{CO}_3(\text{OH})_2$ completely covers the surface of the 20CS coupon in a layered structure, with Fe_3O_4 distributed in the form of nanoparticles within the interspaces of $\text{Fe}_2\text{CO}_3(\text{OH})_2$ layers. As time progresses, the spherical Fe_3O_4 nodules dissolve, failing to stall corrosion advancement.⁴⁴ The CO_2 loading of the saturated BE70H solution significantly surpasses that in the MEAS solution (refer to Figure 2b). Hence, it is reasonable to presume that BEHS contains a larger quantity of CO_3^{2-} and HCO_3^- . This is believed to be beneficial for reacting with dissolved Fe^{2+} to form FeCO_3 .⁴⁴

EDS spectra were performed on the 20CS coupons to investigate the composition of the protective layer, as shown in

Figure 7c,f. The surfaces of the corroded coupons in both BEHS and MEAS solutions mainly consist of Fe, C, and O elements. The highest O content (28.59 wt %) was found in MEAS, indicating that the 20CS coupon may have undergone a more intense oxidation process, forming more iron oxides or other oxygen-containing corrosion products. The results from both the weight loss test and electrochemical experiments confirm that the MEAS solution induces more severe corrosion in 20CS. Thus, it can be inferred that the dense FeCO_3 protective film on 20CS formed in the BEHS solution is more corrosion-resistant than the porous $\text{Fe}_2\text{CO}_3(\text{OH})_2$ film formed in the MEAS solution. This suggests that it is more effective in preventing the spread of corrosion into the metal interior. These findings confirm that the BE70H solution can potentially reduce metal corrosion in the CO_2 capture equipment compared to the MEAS solution.

Our previous work demonstrated that the nonaqueous solvent B1E2 shows negligible formation of $\text{CO}_3^{2-}/\text{HCO}_3^-$ upon CO_2 absorption.¹⁸ These species have been mentioned as critical factors in the 20CS surface film formation. The film formation of 20CS in CO_2 -loaded nonaqueous solvent B1E2 was studied to prove the necessity of $\text{CO}_3^{2-}/\text{HCO}_3^-$ further. It is worth noting that the immersion test is challenging to perform because of the liquid–solid phase transition that

Table 7. DFT Method Calculated the Quantum Chemical Parameters of BDA and MEA Molecules in the Aqueous Phase Based on B3LYP/6-311++G (d,p)

parameters	E_{HOMO} (eV)	E_{LUMO} (eV)	ΔE (eV)	μ (D)	χ (eV)	η (eV)	σ (eV ⁻¹)	ΔN (e)
BDA	-6.6771	-0.0045	6.6762	3.1662	3.3408	3.3363	0.2997	0.5484
MEA	-6.8316	-0.0326	6.7990	1.7664	3.4321	3.3995	0.2503	0.5248

occurs in a CO₂-saturated B1E2 solvent. Therefore, the study employed B1E2 that had absorbed CO₂ for 30 min (B1E2–30), which is near CO₂ saturation (Figure 2b) but remains a clear solution without liquid–solid phase change (Figure S2). Figure S3 illustrates the absence of a significant protective film on the surface of the 20CS coupons submerged in the B1E2–30 solution. The coupon surface appears rough with ridge-like cracks, indicating extensive corrosion of the 20CS surface. As depicted in Figure S3, the XRD results reveal the presence of cementite (Fe₃C) and austenite (γ -Fe), core components of 20CS, on the surface. Because of the absence of an effective protective film, iron consistently leaches during corrosion, gradually exposing the underlying Fe₃C and γ -Fe.⁴⁴ EDS results also show a low content of O elements on the coupon surface (Figure S3), possibly due to the absence of significant iron oxide or ferrous carbonate protective films, allowing the corrosion process to continue. These results indicate that the nonaqueous solvents under study are more corrosive than their aqueous counterparts. If nonaqueous solvents are to be deployed on an industrial scale, the issue of corrosion must be considered. The immersion corrosion experiments and characterization results reveal that H₂O directly impacts the corrosive properties of B1E2. H₂O contributes to the formation of CO₃²⁻/HCO₃⁻ after CO₂ absorption, which is essential for forming an effective protective film to mitigate corrosion at 20CS. Moreover, the absorption experiments show that higher H₂O content in nonaqueous solvents significantly enhances CO₂ loading. Therefore, the introduction of H₂O in nonaqueous solvents will improve the feasibility of the industrial application of these solvents.

3.5. Mechanism. **3.5.1. Corrosion Inhibition Potential of BDA.** The corrosion inhibition properties of amine compounds are based on their adsorption onto metal surfaces, forming a hydrophobic film that significantly reduces the ingress of water and corrosive ions while also slowing down the anodic electrochemical corrosion process of the metal.⁴⁵ Weight loss tests show that B70H has the least corrosivity to 20CS in fresh solutions (Figure 3). Given that it has the same amine concentration as 30 wt % MEA, it is reasonable to speculate that BDA molecules may have higher corrosion inhibition capabilities. Therefore, quantum chemical calculations were executed for the aqueous phase's protonated forms of BDA and MEA molecules. The optimized molecular structures, HOMOs, LUMOs with contours, and molecular electrostatic potential (MEP) are shown in Figure 8. In order to simplify the object of the study, the corrosion inhibition of amines in the mixed solvent environment of ethylene glycol and H₂O was not considered in this study.

Molecular reactivity is analyzed via frontier molecular orbital (FMO) interactions involving the HOMO and the LUMO. A higher E_{HOMO} and a lower E_{LUMO} suggest enhanced molecular adsorption on the metal surface, which is expected to result in superior corrosion inhibition efficiency.⁴⁶ Figure 8c,d demonstrates that the E_{HOMO} values of BDA and MEA were -6.6771 and -6.8316 eV, respectively. However, the E_{LUMO} value of BDA was also higher than MEA's. Given this, the energy gap

($\Delta E = E_{\text{HOMO}} - E_{\text{LUMO}}$) and dipole moment (μ), as shown in Table 7, are further employed to assess the adsorption of amines on the carbon steel surface to predict their corrosion inhibition efficiency. ΔE is an important parameter to measure molecular reactivity and is used to evaluate the electron dynamics and reactivity between molecules and metal surfaces, which is very important in evaluating corrosion inhibition efficiency.⁴⁷ This energy gap is often a more predictive and comprehensive metric than isolated E_{HOMO} and E_{LUMO} values. In addition, the dipole moment (μ), which reflects the electron distribution within the molecule and bond polarity, indicates the direction of corrosion process inhibition.⁴⁸ Lower ΔE values and higher μ values are indicators of enhanced corrosion inhibition performance for molecules.⁴⁹ With a decrease in ΔE , the reactivity of the molecule is elevated, thereby enhancing its corrosion inhibition efficiency. BDA has a lower ΔE than MEA and a higher dipole moment (3.1662 D), suggesting superior corrosion inhibition efficiency than MEA. Global hardness (η) and softness (σ) significantly indicate molecular stability and reactivity. BDA exhibits a lower η but a higher σ than MEA, suggesting that the interaction between BDA molecules and 20CS surface atoms exceeds that of MEA, offering superior adsorption capacity, as shown in Table 7. ΔN signifies the electron transfer number. When $\Delta N < 3.6$, the metal surface's electron-donating ability enhances the corrosion inhibition efficiency of the inhibitor molecule.⁵⁰ BDA and MEA exhibit ΔN values of 0.5484 and 0.5248 e , respectively, suggesting that BDA molecules donate more electrons in interacting with the 20CS surface. MEP provides a visualization of the electron density, aiding in identifying electrophilic and nucleophilic attack sites. As shown in Figure 8e,f, the red areas represent regions with the most negative electrostatic potential, while the blue regions indicate the most positive electrostatic potential. Specifically, the red areas correspond to the highest occupied molecular orbitals of the amine molecules, whereas the blue areas represent the lowest unoccupied molecular orbitals. BDA shows a more extensive red region than MEA, indicating a greater tendency for electron donation and consequently superior adsorption onto the 20CS surface.

In this study, amine molecules function as electron donors, with 20CS acting as an acceptor. The two interact to form an adsorption layer acting as a corrosion inhibitor before the CO₂ absorption. All theoretical results support BDA's corrosion inhibition efficiency being stronger than that of MEA, consistent with the lower CR of the B70H solution observed in weight loss tests (Figure 3a). This could be attributed to the longer hydrocarbon chain and higher molecular weight of BDA, which consequently enhance its adsorption capability on the 20CS surface.⁵¹ This adsorption behavior involves chemisorption and physical adsorption and finally forms a hydrophobic layer to avoid direct contact between the corrosive medium and the 20CS. The chemisorption occurs as heteroatoms like N and O contribute lone pairs of electrons that readily fill the vacant 3d orbitals of Fe atoms, forming coordination covalent bonds with the 20CS surface.⁵²

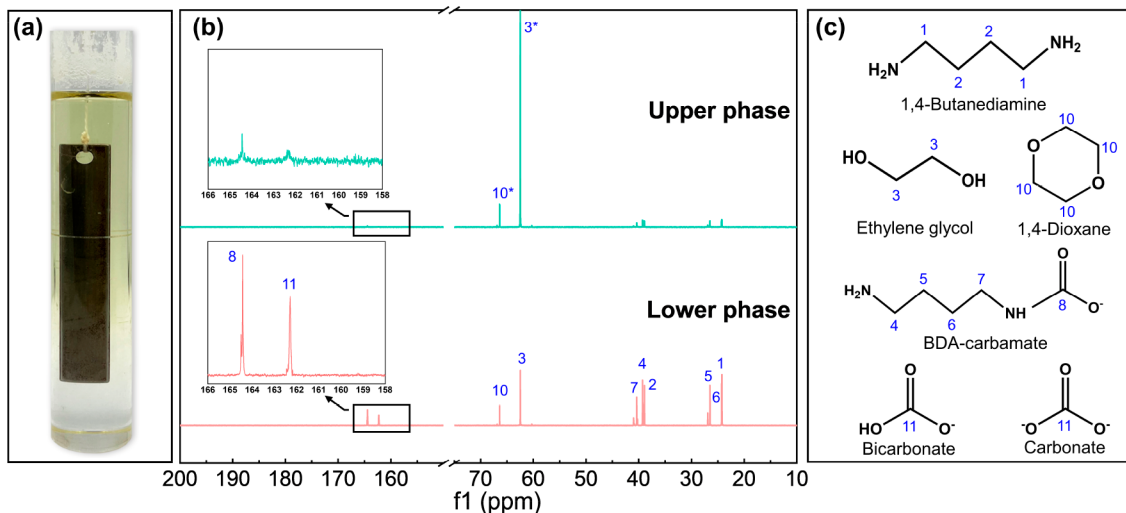


Figure 9. (a) Photo of phase separation phenomenon in BEHS solution, (b) ^{13}C NMR spectra of upper phase and lower phase of the BEHS solution, and (c) main species of BEHS solution.

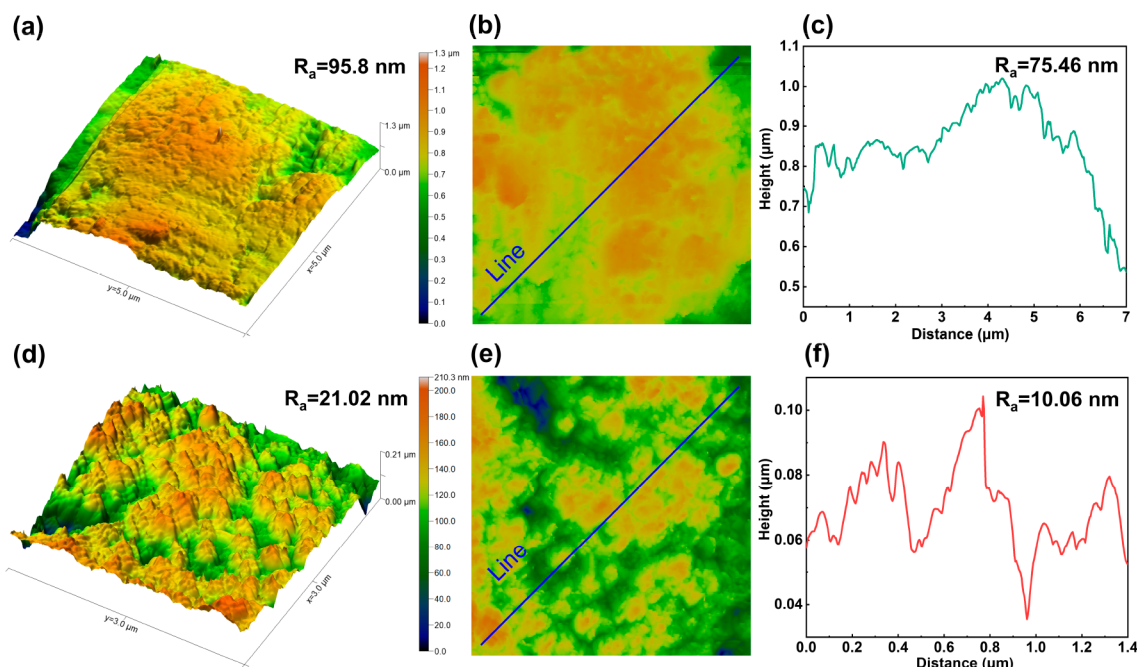


Figure 10. Surface morphology and roughness of 20CS immersed in the upper (a–c) and lower (d–f) phases of BEHS solution for 144 h.

3.5.2. Corrosion Mechanism. Figure 9a depicts the BEHS solution after the weight loss test, showing a yellow-green hue in the upper layer, possibly due to free Fe^{2+} and Fe^{3+} ions, while the lower layer remains clear. Based on these observations, we hypothesize that the solution undergoes phase separation after CO_2 absorption, a phenomenon observed in similar amine/alcohol/water systems such as TETA/DEEA/n-propanol/ H_2O ⁵³ and DETA/1-propanol/ H_2O .²⁶ Therefore, ^{13}C NMR analysis was conducted to determine the species distribution in the upper and lower phases of the BEHS solution, as shown in Figure 9b,c.

In the fresh BE70H solution, the carbon signal at 62.53 ppm corresponded to $-\text{CH}_2$ in EG, and the signals at 40.44 and 29.12 ppm were assigned to $-\text{CH}_2$ in BDA (Figure S4). The upper phase of the saturated BEHS solution exhibits a high signal intensity for the EG peak (carbon atom number 3*)

while the signal strengths for the BDA and carbonate species are notably weak. Almost no peaks from BDA-carbamate (carbon atom numbers 4–8) or from $\text{CO}_3^{2-}/\text{HCO}_3^-$ (carbon atom number 11) could be observed. However, in the lower phase, significant peaks from BDA-carbamate and $\text{CO}_3^{2-}/\text{HCO}_3^-$ were visible. The difference in the substance distribution in the upper and lower phases indicates liquid–liquid separation in the CO_2 -saturated BE70H solution. The upper phase, characterized by low CO_2 loading, primarily comprises water and the physical solvent EG. The lower phase is the CO_2 -rich phase, with absorption products (BDA-carbamate, $\text{CO}_3^{2-}/\text{HCO}_3^-$) primarily concentrated therein. This phase separation behavior may cause corrosion differences in the 20CS coupons.

The upper and lower phases of the corrosion of 20CS carbon steel were evaluated through atomic force microscopy

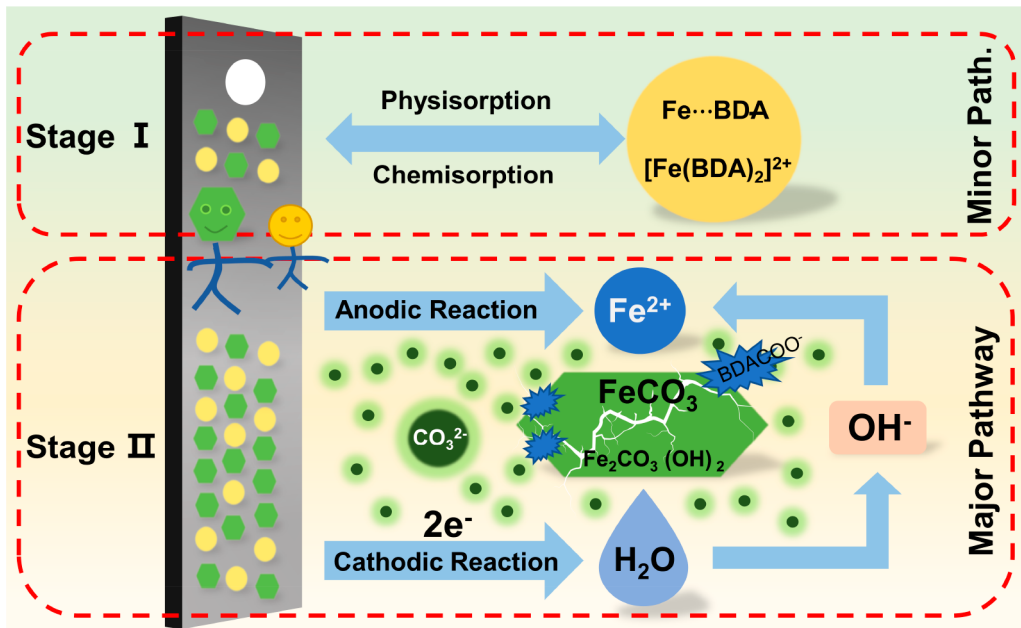


Figure 11. Corrosion and corrosion inhibition mechanisms of 20CS in the BDA/EG/H₂O–CO₂ system.

(AFM) characterization (Figure 10). The 20CS coupons were soaked in the upper and lower phase solutions for 144 h, and these two coupons were respectively termed CS-U and CS-L. The three-dimensional (3D) and two-dimensional (2D) AFM patterns of CS-L appeared smoother than those of CS-U, as shown in Figure 10. The surface of CS-U exhibited significant roughness with a R_a value as high as 95.8 nm, indicating severe surface corrosion (Figure 10a). The R_a value of CS-L was significantly reduced to 21.02 nm (Figure 10d), which could be attributed to the rich CO₂ absorption products in the lower phase, effectively slowing the corrosion of the 20CS surface. In addition, the layered stacking morphology displayed on the CS-L surface in Figure 10d suggests dense protective film formation. The height distribution diagram shows that most areas on the CS-L surface have a relative height between 50 and 90 nm (Figure 10f), indicating a multilayered, overlapping morphology. These results further substantiate the formation of a densely covered protective film on the corroded CS-L surface.

The results from NMR and AFM tests indicate a higher corrosiveness of the upper phase towards 20CS compared to the lower phase. Two main factors account for this: First, there are only trace amounts of CO₃²⁻/HCO₃⁻ species in the upper phase solution, which is not conducive to forming a dense FeCO₃ protective film. Second, the ethylene glycol (EG) in the upper phase is highly corrosive to carbon steel.⁵⁴ This corrosion difference was not evident in the SEM and EDS characterization results, as shown in Figure S6 (upper phase) and Figure 7 (lower phase). In addition, previous studies have shown that a protective film is more easily formed on the steel surface in an amine solution with a higher CO₃²⁻/HCO₃⁻ content.⁴⁴ However, the abundant BDA-carbamate in the lower phase is thought to promote corrosion by disrupting the protective film.¹² Figure 7a,b shows that the 20CS surface in the lower phase experiences lower levels of corrosion and features a dense FeCO₃ protective film. This suggests that within the limited experimental time (144 h), the BDA-carbamate in the lower phase was insufficient to disrupt the already-formed FeCO₃ protective film. The immersion

corrosion test in this study may not be effective in determining the long-term corrosion behavior of 20CS, which will be considered in subsequent work.

According to the results of experiments and literature reports, an interfacial corrosion mechanism between the 20CS surface and the CO₂-loaded BE70H solution is proposed. This involves the following reactions:

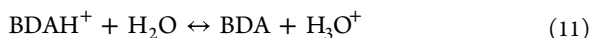
(i) CO₂ reacts with a BE70H solution:



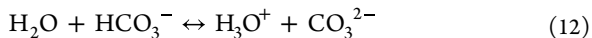
BDACOO⁻ hydrolysis



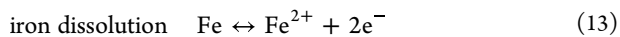
dissociation of protonated amine



dissociation of bicarbonate ion

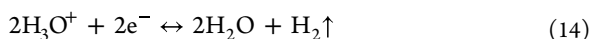


(ii) The main reaction of the anode is the dissolution of Fe in 20CS:⁵⁵

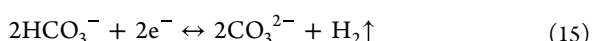


(iii) The BE70H solution in this study was in an anoxic environment, so H₃O⁺, HCO₃⁻, and H₂O were oxidants. There are three main reduction reactions in the cathodes:⁴²

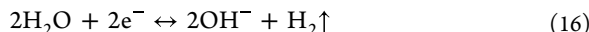
reduction of hydronium ion



reduction of bicarbonate ion



reduction of undissociated water

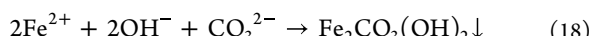


(iv) Based on EDS spectra and XRD results, the main corrosion products are identified as FeCO_3 and $\text{Fe}_2\text{CO}_3(\text{OH})_2$, with the relevant chemical reactions shown in eqs 17 and 18. The initial stages of iron dissolution and film formation are considered to be a dynamic equilibrium process. The formation of corrosion products FeCO_3 and $\text{Fe}_2\text{CO}_3(\text{OH})_2$ consumes partially dissolved iron, promoting further iron dissolution from the 20CS. However, as precipitates continuously cover and accumulate on the surface of the 20CS, the dissolution of iron becomes increasingly hindered. Ultimately, a uniform and effective FeCO_3 film covers the entire 20CS surface, preventing further dissolution of iron. The corrosion system can reach or approach a balanced state at this stage. In addition, owing to its potent iron-chelating properties, carbamate is believed to directly participate in electrochemical processes, which can prevent the formation of protective films or destroy those already formed (eq 19).^{8,12}

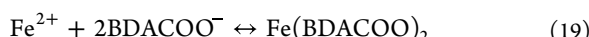
formation of ferrous carbonate



formation of $\text{Fe}_2\text{CO}_3(\text{OH})_2$



formation of compound



Two pathways are believed to mitigate the surface corrosion of 20CS by amine solutions: (i) The formation of a protective layer through the coordination interaction and adsorption of BDA with the carbon steel surface represents a minor pathway for corrosion inhibition, which occurs before CO_2 absorption (stage I). (ii) After absorption, the corrosion products FeCO_3 and $\text{Fe}_2\text{CO}_3(\text{OH})_2$ on the 20CS surface create an additional dense protective film (stage II). This is identified as the major pathway of corrosion inhibition. The role of H_2O in this process is critical as it directly impacts the formation of the $\text{CO}_3^{2-}/\text{HCO}_3^-$ species. In addition, the phase separation behavior of the BEHS solution leads to differences in corrosion at different locations of 20CS coupons, which is related to the distribution of CO_2 absorption products in the upper and lower phase. Figure 11 illustrates the detailed corrosion and inhibition process mechanism based on the analysis above.

4. CONCLUSIONS

This article studied the corrosion behavior of 20CS in a BDA/EG/70 wt % H_2O ternary amine aqueous solution. The weight loss test and ICP-OES analysis results showed that the CR of 20CS in all fresh solutions was nearly 0 mm a^{-1} . In the saturated solution, the CR of 20CS in BEHS was 0.2001 mm a^{-1} , significantly lower than that in MEAS. The electrochemical results show that charge transfer controls the corrosion behavior of 20CS, and BEHS is less corrosive than MEAS, consistent with the weight loss test results. Characterization revealed that the dense siderite (FeCO_3) film on 20CS in BEHS was more corrosion-resistant than the chukanovite ($\text{Fe}_2\text{CO}_3(\text{OH})_2$) film in MEAS, hindering corrosion progression. The presence of H_2O allows the nonaqueous solvent

to generate sufficient $\text{CO}_3^{2-}/\text{HCO}_3^-$ species after CO_2 absorption, which is closely related to film formation. This indicates that the presence of H_2O is expected to improve the corrosion resistance of nonaqueous solvents. Quantum chemistry calculations showed that BDA had higher corrosion inhibition properties than MEA because it could adsorb more effectively on the surface of 20CS, forming a hydrophobic protective layer. This is considered to be a pathway to inhibit the corrosion of 20CS before absorption. NMR results showed that the BEHS solution exhibited phase separation behavior, and the CO_2 -lean phase (upper phase) and CO_2 -rich phase (lower phase) had different corrosion effects on 20CS. The design of CO_2 capture equipment using these biphasic solvents must account for these corrosion differences.

ASSOCIATED CONTENT

Supporting Information

The Supporting Information is available free of charge at <https://pubs.acs.org/doi/10.1021/acs.energyfuels.3c02256>.

Detailed information about the chemicals used in this study, the characterization of 20# carbon steel, visual changes during the liquid–solid phase transition, and the ^{13}C NMR spectra of the fresh amine-based solution (PDF)

AUTHOR INFORMATION

Corresponding Author

Jianzhong Zhu – Key Laboratory of Integrated Regulation and Resource Development on Shallow Lakes, Ministry of Education, College of Environment, Hohai University, Nanjing 210098, China; Email: zhuhhai2010@hhu.edu.cn

Authors

Cunshi Wang – Key Laboratory of Integrated Regulation and Resource Development on Shallow Lakes, Ministry of Education, College of Environment, Hohai University, Nanjing 210098, China; orcid.org/0000-0002-6939-1666

Qiaozhu Zhu – Key Laboratory of Integrated Regulation and Resource Development on Shallow Lakes, Ministry of Education, College of Environment, Hohai University, Nanjing 210098, China

Zhimin Gao – Key Laboratory of Integrated Regulation and Resource Development on Shallow Lakes, Ministry of Education, College of Environment, Hohai University, Nanjing 210098, China

Liang Chen – Management Division of Qinhuai River Hydraulic Engineering of Jiangsu Province, Nanjing 210029, China

Jianlong Liu – Management Division of Qinhuai River Hydraulic Engineering of Jiangsu Province, Nanjing 210029, China

Wangjun Bai – Hohai University Design Institute Co., Ltd., Nanjing 210098, China

Complete contact information is available at: <https://pubs.acs.org/10.1021/acs.energyfuels.3c02256>

Notes

The authors declare no competing financial interest.

ACKNOWLEDGMENTS

This work was supported by the National Natural Science Foundation of China (51979077), the Fundamental Research Funds for the Central Universities, the World-Class Universities (Disciplines), the Characteristic Development Guidance Funds for the Central Universities, the National Scholarship Fund, and the Water Science and Technology of Jiangsu Province (2022036).

REFERENCES

- (1) Zou, C.; Xiong, B.; Xue, H.; Zheng, D.; Ge, Z.; Wang, Y.; Jiang, L.; Pan, S.; Wu, S. The role of new energy in carbon neutral. *Petroleum Exploration and Development* **2021**, *48* (2), 480–491.
- (2) Fernandez, E. S.; Goetheer, E. L.; Manzolini, G.; Macchi, E.; Rezvani, S.; Vlugt, T. J. Thermodynamic assessment of amine based CO₂ capture technologies in power plants based on European Benchmarking Task Force methodology. *Fuel* **2014**, *129*, 318–329.
- (3) Xiao, G.; Xiao, P.; Hoadley, A.; Webley, P. Integrated adsorption and absorption process for post-combustion CO₂ capture. *Front. Chem. Sci. Eng.* **2021**, *15* (3), 483–492.
- (4) Wang, C.; Hua, Y.; Nadimi, S.; Hu, Q.; Taleb, W.; Zhang, J.; Liu, X.; Zhang, R.; Chen, X.; Neville, A.; et al. Anti-corrosion characteristics of FeCO₃ and Fe_xCa_yMg_zCO₃ scales on carbon steel in high-PT CO₂ environments. *Chem. Eng. J.* **2022**, *431*, No. 133484.
- (5) Zhao, Y.; Qi, W.; Xie, J.; Chen, Y.; Zhang, T.; Xu, D.; Wang, F. Investigation of the failure mechanism of the TG-201 inhibitor: Promoting the synergistic effect of HP-13Cr stainless steel during the well completion. *Corros. Sci.* **2020**, *166*, No. 108448.
- (6) Hasib-ur-Rahman, M.; Bouteldja, H.; Fongarland, P.; Siaj, M.; Larachi, F. Corrosion behavior of carbon steel in alkanolamine/room-temperature ionic liquid based CO₂ capture systems. *Ind. Eng. Chem. Res.* **2012**, *51* (26), 8711–8718.
- (7) Bihong, L.; Kexuan, Y.; Xiaobin, Z.; Zuoming, Z.; Guohua, J. 2-Amino-2-methyl-1-propanol based non-aqueous absorbent for energy-efficient and non-corrosive carbon dioxide capture. *Appl. Energy* **2020**, *264*, No. 114703.
- (8) Wu, K.; Zhou, X.; Wu, X.; Lv, B.; Jing, G.; Zhou, Z. Understanding the corrosion behavior of carbon steel in amino-functionalized ionic liquids for CO₂ capture assisted by weight loss and electrochemical techniques. *Int. J. Greenh. Gas Control* **2019**, *83*, 216–227.
- (9) Zheng, L.; Landon, J.; Matin, N. S.; Thomas, G. A.; Liu, K. Corrosion mitigation via a pH stabilization method in monoethanolamine-based solutions for post-combustion CO₂ capture. *Corros. Sci.* **2016**, *106*, 281–292.
- (10) Fischer, K. B.; Daga, A.; Hatchell, D.; Rochelle, G. T. MEA and piperazine corrosion of carbon steel and stainless steel. *Energy Procedia* **2017**, *114*, 1751–1764.
- (11) Gao, M.; Pang, X.; Gao, K. The growth mechanism of CO₂ corrosion product films. *Corros. Sci.* **2011**, *53* (2), 557–568.
- (12) Li, X.; Pearson, P.; Yang, Q.; Puxty, G.; Feron, P.; Xiao, D. A study of designer amine 4-amino-1-propyl-piperidine against the corrosion of carbon steel for application in CO₂ capture. *Int. J. Greenh. Gas Control* **2020**, *94*, No. 102929.
- (13) Cousins, A.; Ilyushechkin, A.; Pearson, P.; Cottrell, A.; Huang, S.; Feron, P. H. M. Corrosion coupon evaluation under pilot-scale CO₂ capture conditions at an Australian coal-fired power station. *Greenhouse Gases: Science and Technology* **2013**, *3* (3), 169–184.
- (14) Pandarinathan, V.; Lepková, K.; van Bronswijk, W. Chukanovite (Fe₂(OH)₂CO₃) identified as a corrosion product at sand-deposited carbon steel in CO₂-saturated brine. *Corros. Sci.* **2014**, *85*, 26–32.
- (15) Zheng, L.; Landon, J.; Matin, N.; Li, Z.; Qi, G.; Liu, K. Corrosion Behavior of Carbon Steel in Piperazine Solutions for Post-Combustion CO₂ Capture. *ECS Trans.* **2014**, *61* (20), 81.
- (16) Zheng, L.; Matin, N. S.; Landon, J.; Thomas, G. A.; Liu, K. CO₂ loading-dependent corrosion of carbon steel and formation of corrosion products in anoxic 30wt.% monoethanolamine-based solutions. *Corros. Sci.* **2016**, *102*, 44–54.
- (17) Finšgar, M.; Jackson, J. Application of corrosion inhibitors for steels in acidic media for the oil and gas industry: A review. *Corros. Sci.* **2014**, *86*, 17–41.
- (18) Wang, C.; Xiao, G.; Zhou, X.; Zhu, Q.; Chen, Y.; Gao, Z.; Liu, C.; Zhu, J. The formation of high CO₂ loading solid phase from 1,4-butanediamine/ethylene glycol biphasic solvent: Phase-changing behavior and mechanism. *Sep. Purif. Technol.* **2023**, *323*, No. 124397.
- (19) Hamborg, E. S.; Derkx, P. W. J.; van Elk, E. P.; Versteeg, G. F. Carbon dioxide removal by alkanolamines in aqueous organic solvents. A method for enhancing the desorption process. *Energy Procedia* **2011**, *4*, 187–194.
- (20) Lin, P.-H.; Wong, D. S. H. Carbon dioxide capture and regeneration with amine/alcohol/water blends. *Int. J. Greenh. Gas Control* **2014**, *26*, 69–75.
- (21) Sharifalhosseini, Z.; Entezari, M. H.; Davoodi, A.; Shahidi, M. Surface modification of mild steel before acrylic resin coating by hybrid ZnO/GO nanostructures to improve the corrosion protection. *J. Ind. Eng. Chem.* **2020**, *83*, 333–342.
- (22) Pearson, R. G. Absolute electronegativity and hardness: application to inorganic chemistry. *Inorg. Chem.* **1988**, *27* (4), 734–740.
- (23) Tao, M.; Xu, N.; Gao, J.; Zhang, W.; Li, Y.; Bernards, M. T.; Shi, Y.; He, Y.; Pan, H. Phase-change mechanism for capturing CO₂ into an environmentally benign nonaqueous solution: A combined NMR and molecular dynamics simulation study. *Energy Fuels* **2019**, *33* (1), 474–483.
- (24) Barbarossa, V.; Barzaghi, F.; Mani, F.; Lai, S.; Stoppioni, P.; Vanga, G. Efficient CO₂ capture by non-aqueous 2-amino-2-methyl-1-propanol (AMP) and low temperature solvent regeneration. *RSC Adv.* **2013**, *3* (30), 12349–12355.
- (25) Tu, Z.; Han, F.; Liu, C.; Wang, Y.; Wei, J.; Zhou, X. 2-Amino-2-methyl-1-propanol regulated triethylenetetramine-based nonaqueous absorbents for solid-liquid phase-change CO₂ capture: Formation of crystalline powder products and mechanism analysis. *Sep. Purif. Technol.* **2023**, *307*, No. 122722.
- (26) Li, X.; Liu, J.; Jiang, W.; Gao, G.; Wu, F.; Luo, C.; Zhang, L. Low energy-consuming CO₂ capture by phase change absorbents of amine/alcohol/H₂O. *Sep. Purif. Technol.* **2021**, *275*, No. 119181.
- (27) Jing, G.; Liu, F.; Lv, B.; Zhou, X.; Zhou, Z. Novel ternary absorbent: Dibutylamine aqueous-organic solution for CO₂ capture. *Energy Fuels* **2017**, *31* (11), 12530–12539.
- (28) Brea, U.; Gómez-Díaz, D.; Navaza, J. M.; Rumbo, A. Carbon dioxide chemical absorption in non-aqueous solvents by the presence of water. *Journal of the Taiwan Institute of Chemical Engineers* **2019**, *102*, 250–258.
- (29) Gonzalez, J. J.; Alfonso, M. E.; Pellegrino, G.. Corrosion of carbon steels in monoethylene glycol. In CORROSION 2000; OnePetro: 2000.
- (30) Singh, R. Relational embeddedness, orientation and relationship quality in emerging markets. *Asia Pacific Journal of Marketing and Logistics* **2008**, *20* (4), 479–492.
- (31) Li, Y.; Cheng, J.; Hu, L.; Liu, J.; Zhou, J.; Cen, K. Phase-changing solution PZ/DMF for efficient CO₂ capture and low corrosiveness to carbon steel. *Fuel* **2018**, *216*, 418–426.
- (32) Hasib-ur-Rahman, M.; Siaj, M.; Larachi, F. CO₂ capture in alkanolamine/room-temperature ionic liquid emulsions: A viable approach with carbamate crystallization and curbed corrosion behavior. *Int. J. Greenh. Gas Control* **2012**, *6*, 246–252.
- (33) Kittel, J.; Fleury, E.; Vuillemin, B.; Gonzalez, S.; Ropital, F.; Oltra, R. Corrosion in alkanolamine used for acid gas removal: From natural gas processing to CO₂ capture. *Mater. Corros.* **2012**, *63* (3), 223–230.
- (34) Hasib-ur-Rahman, M.; Bouteldja, H.; Fongarland, P.; Siaj, M.; Larachi, F. Corrosion behavior of carbon steel in alkanolamine/room-temperature ionic liquid based CO₂ capture systems. *Ind. Eng. Chem. Res.* **2012**, *51* (26), 8711–8718.

- (35) Gunasekaran, P.; Veawab, A.; Aroonwilas, A. Corrosivity of amine-based absorbents for CO₂ capture. *Energy Procedia* **2017**, *114*, 2047–2054.
- (36) Hasib-ur-Rahman, M.; Larachi, F. Prospects of using room-temperature Ionic liquids as corrosion inhibitors in aqueous ethanamine-based CO₂ capture solvents. *Ind. Eng. Chem. Res.* **2013**, *52* (49), 17682–17685.
- (37) Krzemień, A.; Więckol-Ryk, A.; Smoliński, A.; Koteras, A.; Więsław-Solny, L. Assessing the risk of corrosion in amine-based CO₂ capture process. *Journal of Loss Prevention in the Process Industries* **2016**, *43*, 189–197.
- (38) Nainar, M.; Veawab, A. Corrosion in CO₂ capture unit using MEA-piperazine blends. *Energy Procedia* **2009**, *1* (1), 231–235.
- (39) Veawab, A.; Tontiwachwuthikul, P.; Chakma, A. Corrosion behavior of carbon steel in the CO absorption process using aqueous amine solutions. *Ind. Eng. Chem.* **1999**, *38* (10), 3917–3924.
- (40) Siğircik, G.; Tüken, T.; Erbil, M. Assessment of the inhibition efficiency of 3,4-diaminobenzonitrile against the corrosion of steel. *Corros. Sci.* **2016**, *102*, 437–445.
- (41) Lebrini, M.; Lagrenée, M.; Vezin, H.; Traisnel, M.; Bentiss, F. Experimental and theoretical study for corrosion inhibition of mild steel in normal hydrochloric acid solution by some new macrocyclic polyether compounds. *Corros. Sci.* **2007**, *49* (5), 2254–2269.
- (42) Xiang, Y.; Xie, W.; Ni, S.; He, X. Comparative study of A106 steel corrosion in fresh and dirty MEA solutions during the CO₂ capture process: Effect of NO₃⁻. *Corros. Sci.* **2020**, *167*, No. 108521.
- (43) Zheng, L.; Landon, J.; Zou, W.; Liu, K. Corrosion benefits of piperazine as an alternative CO₂ capture solvent. *Ind. Eng. Chem. Res.* **2014**, *53* (29), 11740–11746.
- (44) Xu, Y.; Yang, Q.; Seeber, A.; Yu, H.; Wang, T.; Puxty, G.; Fang, M. The impact of novel diamine based aqueous and water lean solvents on the corrosion of carbon steel. *Corros. Sci.* **2023**, *210*, No. 110816.
- (45) Migahed, M. A.; Attia, A. A.; Habib, R. E. Study on the efficiency of some amine derivatives as corrosion and scale inhibitors in cooling water systems. *RSC Adv.* **2015**, *5* (71), 57254–57262.
- (46) El Adnani, Z.; McHarfi, M.; Sfaira, M.; Benzakour, M.; Benjelloun, A. T.; Ebn Touhami, M. DFT theoretical study of 7-R-3methylquinoxalin-2(1H)-thiones (RH; CH₃; Cl) as corrosion inhibitors in hydrochloric acid. *Corros. Sci.* **2013**, *68*, 223–230.
- (47) Xia, S.; Qiu, M.; Yu, L.; Liu, F.; Zhao, H. Molecular dynamics and density functional theory study on relationship between structure of imidazoline derivatives and inhibition performance. *Corros. Sci.* **2008**, *50* (7), 2021–2029.
- (48) Obot, I. B.; Obi-Egbedi, N. O. Indeno-1-one [2,3-b]quinoxaline as an effective inhibitor for the corrosion of mild steel in 0.5M H₂SO₄ solution. *Mater. Chem. Phys.* **2010**, *122* (2), 325–328.
- (49) Jafari, H.; Danaee, I.; Eskandari, H.; RashvandAvei, M. Electrochemical and theoretical studies of adsorption and corrosion inhibition of N,N'-Bis(2-hydroxyethoxyacetophenone)-2,2-dimethyl-1,2-propanediimine on low carbon steel (API SL Grade B) in acidic solution. *Ind. Eng. Chem. Res.* **2013**, *52* (20), 6617–6632.
- (50) Kovačević, N.; Kokalj, A. The relation between adsorption bonding and corrosion inhibition of azole molecules on copper. *Corros. Sci.* **2013**, *73*, 7–17.
- (51) Malinowski, S.; Wróbel, M.; Woszuk, A. Quantum chemical analysis of the corrosion inhibition potential by aliphatic amines. *Materials* **2021**, *14* (20), 6197.
- (52) Zeng, Y.; Kang, L.; Wu, Y.; Wan, S.; Liao, B.; Li, N.; Guo, X. Melamine modified carbon dots as high effective corrosion inhibitor for Q235 carbon steel in neutral 3.5 wt% NaCl solution. *J. Mol. Liq.* **2022**, *349*, No. 118108.
- (53) Liu, J.; Qian, J.; He, Y. Water-lean triethylenetetramine/N,N-diethylethanamine/n-propanol biphasic solvents: Phase-separation performance and mechanism for CO₂ capture. *Sep. Purif. Technol.* **2022**, *289*, No. 120740.
- (54) Khomami, M. N.; Danaee, I.; Attar, A. A.; Peykari, M. Corrosion of alloy steel in 30% ethylene glycol solution and CrO₂₄ under hydrodynamic condition. *Journal of Iron and Steel Research, International* **2013**, *20* (6), 82–87.
- (55) Veawab, A.; Aroonwilas, A. Identification of oxidizing agents in aqueous amine-CO₂ systems using a mechanistic corrosion model. *Corros. Sci.* **2002**, *44* (5), 967–987.